The Fine-Structure of Nearshore Tidal and Residual Circulations Revealed by H. F. Radar Surface Current Measurements

D. PRANDLE

Institute of Oceanographic Sciences, Bidston Observatory, Birkenhead, Merseyside, L43 7RA, U.K.

(Manuscript received 5 June 1986, in final form 4 September 1986)

ABSTRACT

Using the Ocean Surface Current Radar (OSCR) developed by the Rutherford–Appleton Laboratory (UK), 30 days of synoptic hourly surface current vectors were obtained for 84 locations within a nearshore region some 18 kms square. Tidal analyses of these data show that the currents associated with the predominant M_2 constituent sweep smoothly and regularly through the area, unaffected by the finer topographic features. Moreover, contours of the amplitude of the M_2 semi-major axis are mutually consistent to a precision of better than 0.5 cm s^{-1}. Statistical analyses of these data indicate that the standard error of OSCR current measurements is less than 4 cm s^{-1}. By contrast the major higher harmonic constituent, M_4, shows pronounced, but ordered, spatial variability. Relating the observed distributions for M_4 and M_2 is foreseen as an instructive modeling problem that should advance our knowledge of shallow water tidal interaction processes.

Standard relationships between residual surface currents and the associated wind forcing only accounted for typically 30% of the current variance. However, by using the empirical orthogonal function technique a single mode was found to be responsible for up to 90% of the total variance with a mean value of 66% over the complete set of measurements. While the time-series for the (complex) amplitude of this mode showed significant correlation with the wind-stress time series (0.73 E–W and 0.32 N–S), the former was characterized by much longer period oscillations. The velocity vectors of this mode were almost uniformly aligned but varied in amplitude by a factor of 2. Thus, a low-frequency "slablike" surface current response to wind forcing is indicated. However, this response includes indirect components possibly involving modifications to current structure due to changes in density fields and nearshore influences.

1. Introduction

Measurements of high frequency radar echoes backscattered from the sea surface can be used to deduce information on both waves and surface currents (Barrick, 1978; Shearman, 1983; Leise, 1984). The measured spectra exhibit two peaks corresponding to a resonance between the radio wavelength, λ_R, and both advancing and receding surface waves of length $\lambda_w = \frac{1}{2}\lambda_R$. In still water, these "Bragg" peaks would occur at frequency shifts of $\pm c/\lambda_w$ where c is the wave celerity. Where the waves propagate in a current u, the Bragg peaks are offset by u/λ_w. Since λ_R is known, measurement of the two Bragg peaks enables u to be determined directly without any calibration constants. The Rutherford–Appleton Laboratory (UK) developed a system named OSCR (Ocean Surface Current Radar) (King et al., 1984), based on the CODAR system (Barrick et al., 1977) to measure nearshore surface currents. OSCR uses a beam-forming receiving antenna comprising 16 separate elements equispaced over a line 90 m long oriented orthogonally to the center line of the radar beam coverage. Signals from 16 beams each 6° wide can be differentiated. Along each beam signals can be separated into "bin" lengths of 1.2 km. Operating at a frequency close to 27 mHz measurements can be made over distances up to 40 km offshore. For this frequency $\lambda_w \approx 5$ m and the measured velocity u reflects an integrated value over the near-surface layer effective in advecting waves of this length, i.e., approximately the top meter. The system has been deployed in nine oceanographic experiments over a two year period. Summaries of these experiments have been given by Prandle (1985b) and Prandle and Howarth (1986).

The present experiment was carried out in May–June 1985 following a trial experiment conducted in April 1984. In this earlier experiment, in Liverpool Bay (Prandle and Ryder, 1985), only one OSCR unit was available and measurements from one site were combined with measurements taken one month later from a second site. The coherence of the tidal forcing then enabled the construction of a tidal ellipse distribution for the predominant M_2 constituent. These OSCR results for M_2 were shown to be in close agreement with values derived both from a numerical tidal model and from moored current meters.

Encouraged by these results and the availability of two OSCR units, a dual deployment in Red Wharf Bay (Fig. 1) was planned for a period of 30 days. The location chosen lies within an enclosed shelf sea dominated by strong tidal forcing evidenced by a spring tidal range of 6.5 m and a neap range of 3.4 m. Significant

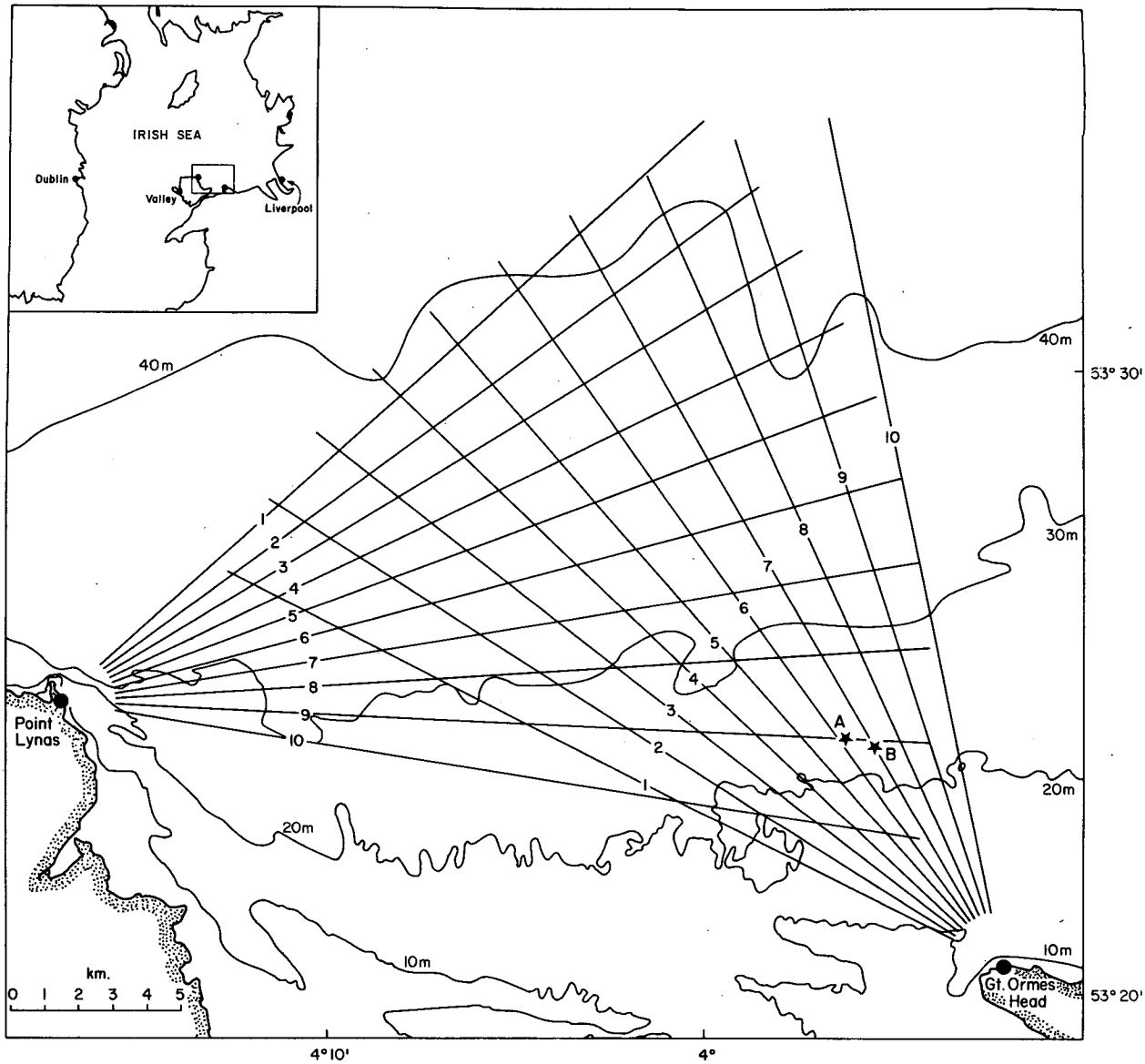

FIG. 1. Red Wharf Bay. Radars located at Pt. Lynas and Orme. Current meters deployed at positions A and B. Wind recorded at Valley.

wind forcing also occurs in this area and, in this respect, the region of radar coverage extended from nearshore sheltered areas to open sea conditions. Depths in the area covered range from 10 to 50 m and hence significant nonlinear interactions occur through the influence of both shallow water and bed friction. Interesting flow features associated with the promontory to the west of the region were also expected. Moreover, the timing of the experiment was chosen to coincide with related experiments concerning the formation of density fronts. Thus, while complete vertical mixing was expected within the region of OSCR coverage some encroachment of fronts in the area immediately east of the OSCR region was anticipated.

One objective concerned a continuing assessment of the performance of the OSCR system. It was also anticipated that the unique spatial coverage of surface currents would reveal interesting facets of nearshore circulation. The results included here fulfill this expectation offering new insights into the mechanics of both tidal and wind-driven phenomena. The present paper extends to the presentation of the essential results in a synthesized form. The ensuing phase, involving more extensive theoretical interpretation of the results, is proceeding and will be presented later.

2. Observations

Concurrent measurements were made at the two sites shown in Fig. 1, from 5 May to 3 June 1985. The mode of operation was as follows:

At one site, backscattered signals pertaining to 20 bins along one beam were recorded for 2 minutes. In the following 3 minutes, these signals were spectrally analyzed and radial currents determined. Concurrently, within this 3 minute interval, backscattered signals were recorded at the other site. This interleaving procedure enabled measurements at one site to be made at 5 minute intervals, allowing measurements along each of 12 separate beams (preselected out of the 16 possible beams) to be made at hourly intervals. Thus, the observational program was designed to provide 30 days of hourly data appropriate to the requirements of accurate tidal analysis.

Alignment of the radar at the Orme site (located on a shelf in a limestone scarp some 100 m above sea level) was restricted. This factor, in combination with the range of 25 km (for the first 20 bins) and the need for beam crossing angles to be greater than about 20° to accurately resolve the current vectors, restricted the determination of current vectors to the area delineated by just 10 beams from each site as shown in Fig. 1.

A number of other instruments were deployed as part of the experimental program. Here, we consider only additional data from 1) a bottom mounted Aanderaa current meter (measuring height 1 m above bed) located at 53°24.1′N, 3°56.3′W deployed for 27 days in May 1985 (position A in Fig. 1; mean water depth approximately 25 m) and 2) a moored Aanderaa current meter deployed for 29 days in April 1977 (measuring height 11 m above bed) located at 53°24.0′N, 3°55.5′W (position B in Fig. 1). Hourly wind data were available from a meteorological station at Valley, shown in Fig. 1.

3. Tidal components

Separate tidal analyses were carried out for the time series of radial currents pertaining to all 20 bins along each of the 20 beams. A version of the Harmonic Method developed at IOS Bidston was used, calculating the amplitude and phase of 27 separate constituents together with an additional 8 related constituents (equilibrium relationships assumed). Use was made of a software package specifically designed (by the Marine Information and Advisory Service of IOS) to expedite the total of 400 tidal analyses, this package also allowed for missing values in the hourly time series. At the same time, residual current components were calculated by simple subtraction of the "tidally predicted signal" from the original time series.

To calculate tidal ellipse properties at the beam intersection points, linear interpolation from the tidal constituents calculated for the nearest bin positions was used. Further consideration of the results of these tidal analyses is restricted to 10 major constituents representative of the four main parts of the tidal spectrum namely 1) semidiurnal, 2) higher harmonics, 3) diurnal and 4) longer period.

Table 1 shows tidal ellipse properties for these 10 major constituents derived from 1) OSCR measurements at the intersection of beams, nine from Pt. Lynas and six from Orme; 2) 30 days of current observations from the meter moored at mid depth at position B (1 km east of A); and 3) 30 days of current observations from the bottom mounted meter at the adjacent position A. This close proximity of A and B allows us to consider these results as representative of the vertical structure of tidal constituents at one point with values from 1) surface, 2) mid depth and 3) bed. Figure 2, parts a, b, c and d respectively, indicate the spatial distributions of tidal ellipse properties obtained from OSCR measurements for the constituents a) M_2, b) M_4, c) O_1 and d) Mm. The parameters amplitude, direction and phase refer to values for the semi-major axis of the ellipse, with direction measured clockwise from North. Eccentricity is defined as the ratio of amplitudes of minor axis: major axis with positive indicating anticlockwise rotation and negative clockwise rotation.

a. Semidiurnal constituents: M_2, N_2, S_2

Table 1 indicates the predominance of the M_2 constituent. For M_2, the current amplitude at mid depth is approximately ¾ surface value while at the bed it is only ⅓ surface value. Similar reduction factors are found for the other two major semidiurnal constituents (N_2 and S_2) and likewise for O_1, K_1 and M_4. For M_2, the 5° phase advance at the bed and the increase in ellipticity from −0.13 at the surface through −0.01 at mid depth to +0.15 at the bed both accord qualitatively with the theoretical estimations for the vertical structure of tidal currents (as derived for a quadratic bed stress and eddy viscosity constant over both time and water depth—Prandle, 1982). The reduction in amplitude at mid depth and the bed also follows from this theory though the extent of the reduction at the bed is probably associated with benthic processes not incorporated in this theory. For all three semidiurnal constituents, the maximum variability between values of both phase and direction from columns 1, 2 and 3 is ±2.5° of the mean.

Detailed examination of the spatial distributions of M_2 tidal ellipse properties (Fig. 2a) indicates a markedly smooth and regular distribution of the amplitude, direction and phase parameters with no anomalies occurring between contours of these parameters. Amplitude increases from 75 cm s^{-1} at the eastern edge to 95 cm s^{-1} at the western edge with an accompanying direction change from 90° to 110°. The phase variation from 221° to 236° reflects a phase advance due to increase in the ratio of friction to inertia terms in shallow water. Eccentricity is clockwise throughout, generally with a value close to −0.1 but increasing (in a clockwise sense) to −0.2 in shallower water.

The S_2 and N_2 ellipse distributions (not shown) are similar in character to that for M_2 with only a slight reduction in the smoothness of the contour distributions. The range of variations in ellipse parameters for

TABLE 1. Tidal ellipse measurements at position A. 1: OSCR near surface, 2: moored current meter at middepth, 3: bottom-mounted current meter. All values calculated from approximately 30 days data. Amplitude, direction and phase refer to semi-major axis. Amplitude is in cm s^{-1}, lower values in parentheses indicate percentage of M_2 value. Direction measured clockwise from north. Eccentricity: minor axis/major axis, +*ve* for anticlockwise rotation and −*ve* for clockwise rotation. Zo represents the mean current averaged over the observational period after removal of all tidal constituents.

Constituent period	Amplitude			Direction			Phase			Ellipticity		
	1	2	3	1	2	3	1	2	3	1	2	3
Zo	9.7 (12)	3.0 (5)	3.8 (14)	0	256	196						
Mm 27.6 d	6.9 (9)	1.5 (3)	1.0 (4)	38	53	308	262	329	5	−0.11	0.35	0.00
MSf 14.8 d	5.0 (6)	1.2 (2)	0.6 (2)	86	59	63	176	307	94	−0.03	−0.53	0.18
O_1 25.82 h	2.2 (3)	0.9 (2)	0.7 (3)	116	120	80	253	312	301	0.03	−0.23	−0.38
K_1 23.94 h	2.0 (3)	1.0 (2)	0.5 (2)	121	71	95	69	76	94	0.07	−0.01	0.04
N_2 12.66 h	16.4 (21)	11.3 (19)	5.4 (20)	103	101	98	196	200	202	−0.18	−0.11	0.20
M_2 12.42 h	79.8 (100)	58.2 (100)	27.4 (100)	99	100	100	226	226	221	−0.13	−0.01	0.15
S_2 12.00 h	26.7 (33)	18.3 (31)	9.0 (33)	103	103	98	258	262	263	−0.03	−0.03	−0.01
M_4 6.21 h	7.6 (10)	5.4 (9)	2.2 (8)	90	98	226	90	104	325	−0.47	0.02	0.19
MS_4 6.10 h	4.9 (6)	3.1 (5)	1.0 (4)	86	96	251	125	158	346	−0.31	0.03	0.38
M_6 4.14 h	3.9 (5)	1.9 (3)	0.4 (1)	118	106	102	297	211	257	−0.19	−0.19	−0.07

10 major constituents, including S_2 and N_2 is shown in Table 2.

b. Higher harmonics M_4, MS_4 and M_6

The tidal ellipses for M_4 are shown in Fig. 2b. The parameters range from: amplitude 6 to 11 cm s^{-1}, direction 60° to 120°, phase 60° to 110°, and eccentricity −0.8 to +0.2. The parameter contours retain spatial coherence with a "pole" close to the 90° phase "island" at which point the eccentricity is zero increasing (in a clockwise sense) radially outwards. Tidal ellipses for MS_4 (not shown) vary in a more irregular manner (see Table 2). When compared with M_4, this more irregular distribution for MS_4 might be a consequence of the increased complexity of the forcing mechanisms involving the interaction of M_2 and S_2 constituents. The regularity of the M_6 ellipse distributions (not shown) lies midway between the patterns for M_4 and MS_4. However, the phase distribution is notably well ordered resulting, perhaps, from a phase locking mechanism with the forcing M_2 constituent.

From Table 1, M_4 amplitudes are close to 10% of M_2 amplitudes for all three datasets. However, for M_4, MS_4 and M_6 direction, phase, and eccentricity show larger variations between surface and bed. This variability may be attributed to (i) complex vertical current structure, (ii) inaccuracy in resolving these constituents or (iii) varying degrees of contamination by surface waves. Similar comments apply to the following tidal species.

c. Diurnals O_1 and K_1

Tidal ellipses for O_1 are shown in Fig. 2c, the range of parameter values is shown in Table 2. The K_1 tidal ellipses (not shown) show a similar range of variation. The current ellipses for both constituents indicate a broad circular sweep of flow around the Pt. Lynas promontory. Theoretically, the O_1 constituent can be accurately resolved from a monthly recording of hourly data, whereas the K_1 values rely on assumed relationships with other constituents. Significant irregularity exhibited in the parameter contours for both O_1 and K_1 suggests that the accuracy of the recordings is barely adequate to determine these constituents. The large variability in parameter values shown in Table 1 between all three datasets suggests that this latter conclusion also applies to the current meter recordings (columns 2 and 3).

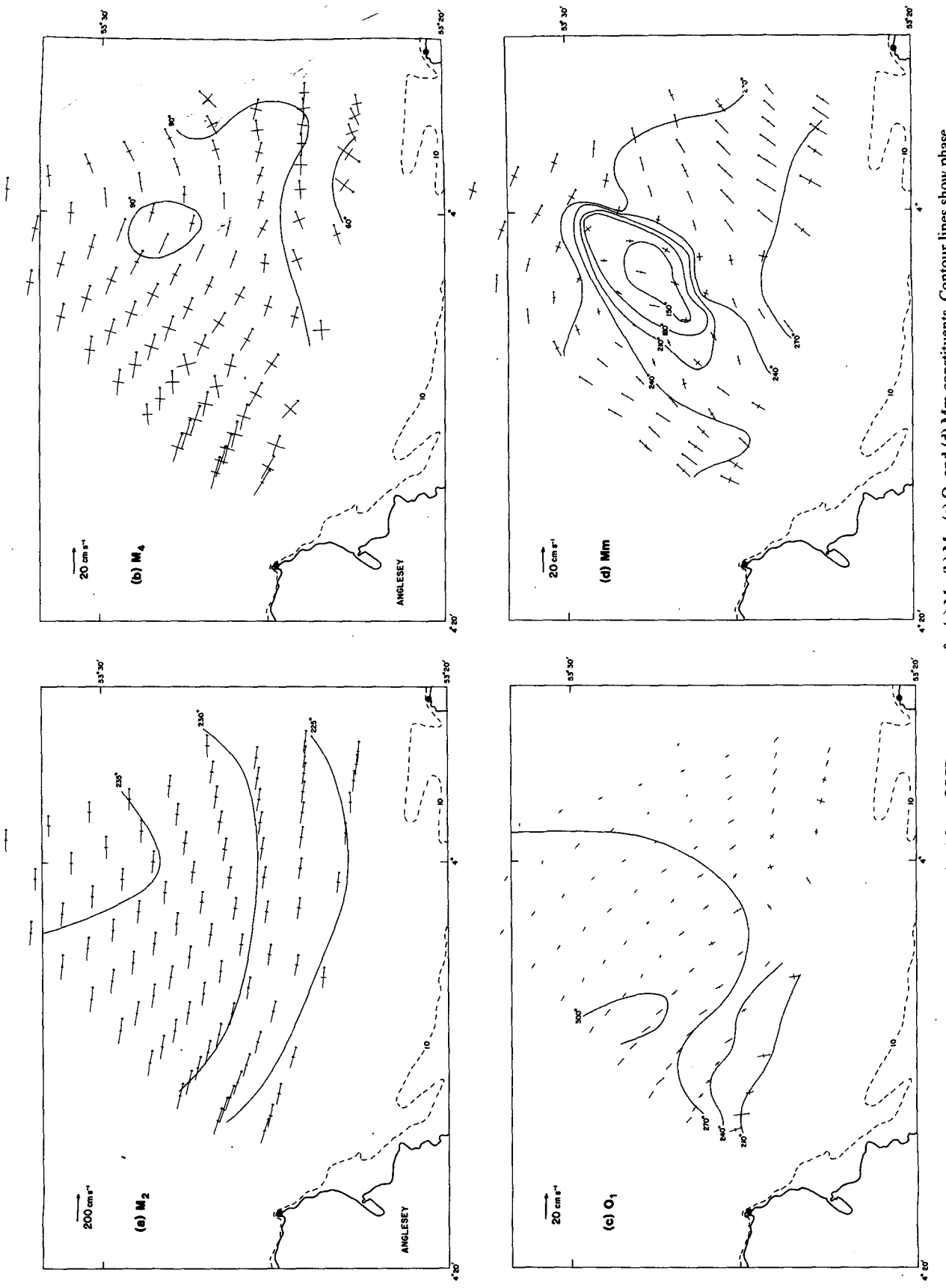

FIG. 2. Distribution of tidal ellipses determined from OSCR measurements for (a) M_2, (b) M_4, (c) O_1 and (d) Mm constituents. Contour lines show phase.

TABLE 2. Range of variation of tidal ellipse parameters over the OSCR region. Parameter definitions as for Table 1.

Constituent	Amplitude	Direction	Phase	Ellipticity
Mm	4–8	30–90	150–270	−0.6 to 0.2
MSf	4–8	90–140	150–180	−0.7 to 0.1
O_1	1–5	120–150	210–300	−0.4 to 0.4
K_1	2–5	90–150	60–100	−0.5 to 0.2
N_2	14–21	80–120	190–210	−0.25 to −0.1
M_2	75–95	90–110	221–236	−0.2 to −0.1
S_2	24–30	95–115	255–275	−0.15 to 0.0
M_4	6–11	60–120	60–110	−0.8 to 0.2
MS_4	4–7	0–150	100–170	−0.3 to 0.0
M_6	2–7	120–210	270–300	−0.7 to 0.2

d. Longer period MSf and Mm

Tidal ellipses for Mm are shown in Fig. 2d and parameter ranges in Table 2. These parameters vary in an irregular fashion except for the ordered phase progression shown. Tidal ellipse distribution for MSf (not shown) are similarly irregular. These constituents cannot be meaningfully resolved from a data series of only one month, the values obtained reflect the time series for surge energy rather than the strict astronomical tidal constituents.

Godin (1972) showed that the accurate resolution of tidal constituents depends on: 1) frequency and duration of the observations, 2) magnitude of the constituent, 3) existence of neighboring constituents and 4) the noise level. The duration of recordings should be such that all major constituents are separated by a frequency difference equivalent to the inverse of the record length. Figure 3 shows the constituents derived from the tidal analysis of bin 19 along beam 9 from Pt. Lynas (approximately the E–W current component at position A). The month-long recording provides accurate separation of constituents spaced more than 0.5 deg h^{-1} and is thus sufficient for most constituents shown.

For well-separated constituents, Godin shows that the accuracy of resolution is given by

$$\Delta A = \nu\sqrt{2/N} \tag{1}$$

$$\Delta g = \nu\sqrt{2/N}/A \quad \text{[rad]} \tag{2}$$

where ΔA is the standard error in the tidal amplitude A, Δg the standard error in the phase g, ν the standard error of the "white" noise, and N the number of observations.

The contoured values for the magnitude of the M_2 major axes indicated mutual consistency to better than 0.5 cm s^{-1}. To obtain a more precise estimate of ΔA and Δg, and thereby to estimate ν from (1) and (2), plots (Fig. 4) were made of the M_2 current ellipse values for amplitude and phase determined at beam intersections along (a) beam 9 from Pt. Lynas and (b) beam 6 from Orme. We then assume that in nature A and g vary smoothly and that departures from the smooth curves (sketched) reflect the respective noise levels. By using ellipse parameters at beam intersections rather than radial components from specific bins, the influence of any small changes in direction of the ellipse major axis associated with localized topography is minimized. The values from Pt. Lynas, beam 9 were ΔA = 0.14 cm s^{-1} and $\Delta g = 0.14°$, suggesting respec-

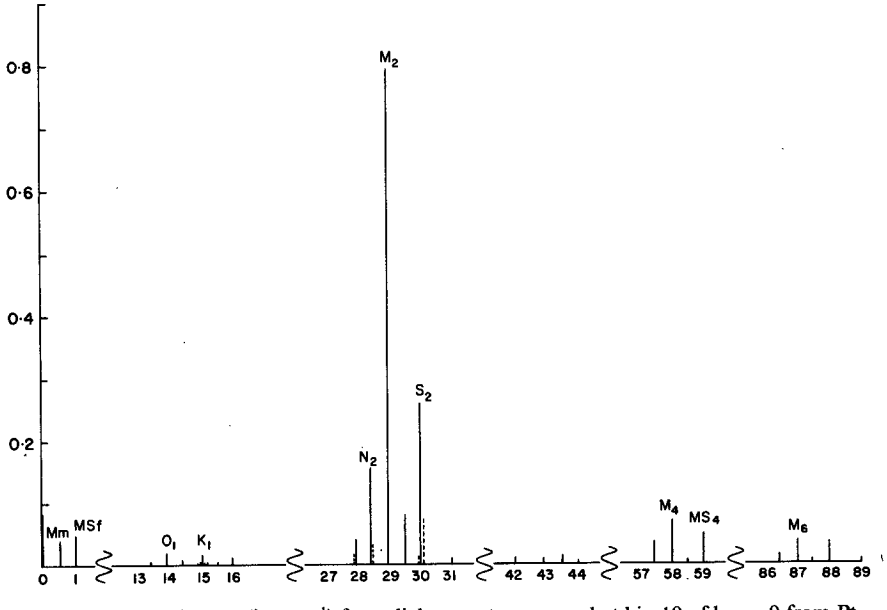

FIG. 3. Tidal constituents (in m s^{-1}) for radial currents measured at bin 19 of beam 9 from Pt. Lynas (close to position A). Tidal frequencies in deg h^{-1}. Dashed lines indicate related constituents.

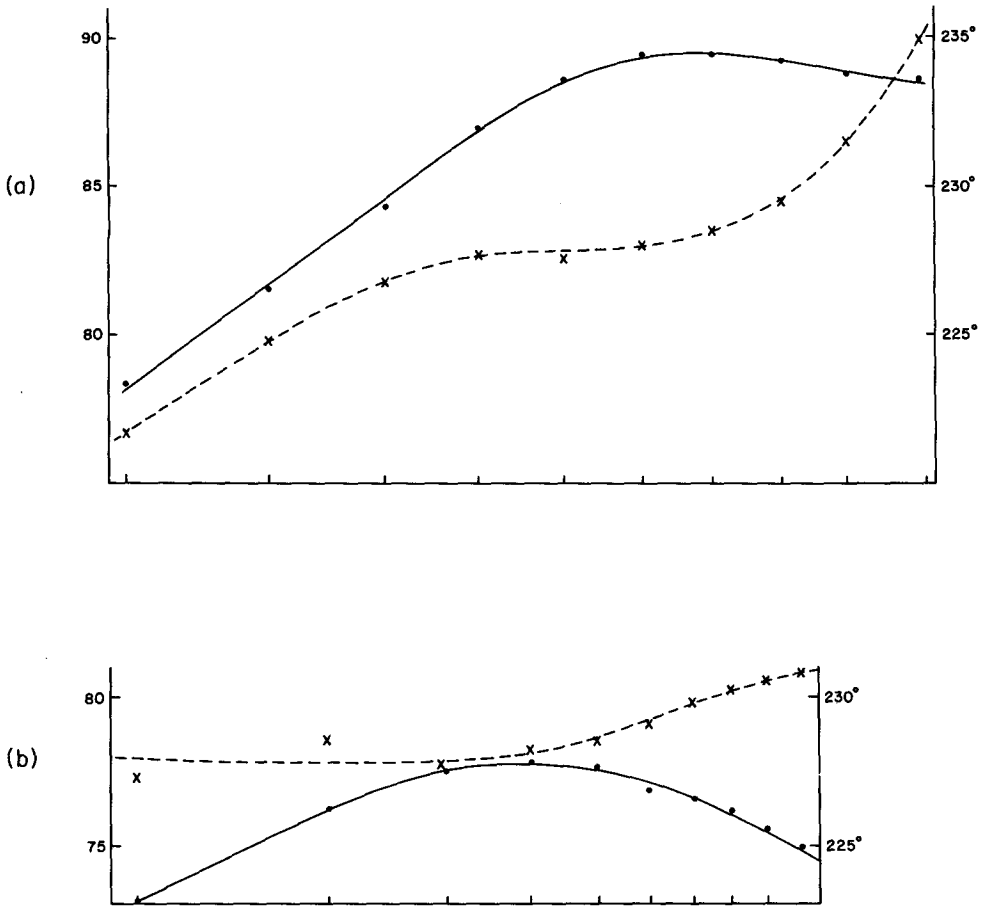

FIG. 4. Variations of M_2 current ellipse values for amplitude (semi-major axis), and phase at beam intersections along (a) beam 9 from Pt. Lynas and (b) beam 6 from Orme: × amplitude, O phase.

tively from (1) and (2) values of ν = 2.5 and 3.8 cm s^{-1}, the latter for a mean value A = 85 cm s^{-1}. Similarly, values from Orme, beam 6 were ΔA = 0.28 cm s^{-1} and Δg = 0.14° with respective values of ν = 5.1 and 3.7 cm s^{-1}, the latter for A = 80 cm s^{-1}. Thus, overall these results suggest a standard error of $\nu \approx 4$ cm s^{-1}. In this simplistic approach, the estimate for ν includes both physical signals and instrumental errors and hence the value should be regarded as a conservative upper limit.

The above procedure suggests that well-separated constituents should be resolved to an accuracy of the order of ±0.25 cm s^{-1} in A and (i) ±1.3° in g for A = 10 cm s^{-1}, or (ii) ±6.5° in g for A = 2 cm s^{-1}. These error estimates for both A and g are consistent with the accuracy of determination of the various tidal constituents described earlier.

4. Residual component

a. Mean values

Figure 5 shows the mean residual vectors, i.e., the time-average of the nontidal (or residual) component. The vectors indicate a northwards surface drift ranging from a maximum of 17 cm s^{-1} in the shallower southern area to about 3 cm s^{-1} in the deeper northern area. The superimposed "streamlines" were calculated by assuming these residual surface currents persist throughout the water column. The net transport indicated of 40 × 10^3 m^3 s^{-1} may be compared with the estimated long-term flow through the Irish Sea of 60 × 10^3 m^3 s^{-1}. This calculated net transport far exceeds fresh water inflow into this region and, almost certainly, the observed residuals represent a surface drift counterbalanced by southward flow close to the bed. Some confirmation for this conclusion is indicated in Table 1. Thus, at position A the northwards surface velocity of 10 cm s^{-1} measured by OSCR is counterbalanced by a southwards near-bed velocity of 4 cm s^{-1} measured by the bottom-mounted current meter.

Residual velocities associated with Stoke's transport (simplified one-dimensional approximation, Pingree and Maddock 1985) can be calculated, for the M_2 constituent, from $\frac{1}{2}(U\hat{Z}/H)\cos\theta_u$ eastwards and $\frac{1}{2}(V\hat{Z}/H)\cos\theta_v$ northwards where $\hat{U}$, $\hat{V}$ and $\hat{Z}$ represent M_2 tidal amplitudes of current components ($\hat{U}$, $\hat{V}$) and of

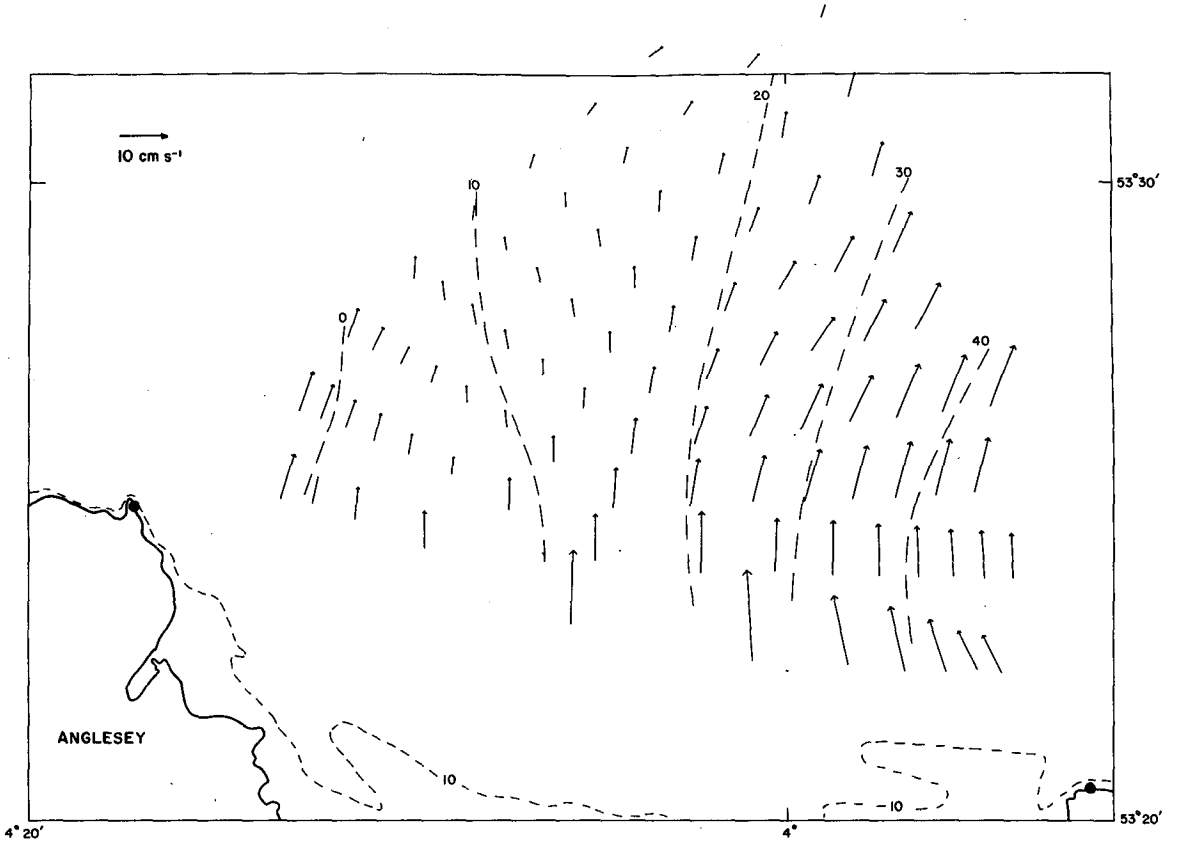

FIG. 5. Observed mean surface current. Contour lines indicate integrated flow in units of 10^3 m^3 s^{-1} (assuming surface drift persists through depth).

elevation $\hat{Z}$; H is the water depth and θ_u, θ_v the phase differences between (i) $\hat{U}$ and $\hat{Z}$ and (ii) $\hat{V}$ and $\hat{Z}$. From Robinson (1979), $\hat{Z}$ = (2.5 m, 307°) ± (0.15, 5°) over the OSCR region, Stoke's drift velocities of up to 0.8 cm s^{-1} eastward and 1.0 cm s^{-1} southward are obtained. Thus, some counterbalancing northward flow component is expected but, even allowing for a variation in the vertical profile of such a flow, it is too small to account for the observed surface drift.

The most likely forcing mechanisms for these large net surface residuals are (i) wind forcing and (ii) horizontal density gradients (the region was thought to be well mixed vertically at the time of the observations). One common assumption for wind-driven surface currents is the "2% law," i.e., the surface drift amounts to 2% of the wind speed. Thus, mean surface drifts of 17 and 3 cm s^{-1} would require, respectively, mean northward wind speeds of 8.5 and 1.5 m s^{-1}. Averaged over the observational period, the mean northwards component of wind speed was (measured at Valley) 2.5 m s^{-1} with a mean westward component of 1.7 m s^{-1}. Thus, while wind is not an insignificant component in forcing the mean surface residual currents, some additional component must be acting to drive the larger observed values.

Using simple one-dimensional theory for tidally dominated regions and assuming zero depth-averaged flow, Prandle (1985a) derived the following formulae for surface velocities due to (i) a wind velocity W and (ii) a longitudinal density gradient

$$\text{wind forcing:} \quad U_w = 0.31\tau_w/\rho k\hat{U} \tag{3}$$

$$\text{density gradient:} \quad U_p = 0.036gH^2\frac{(\partial\rho/\partial x)}{\rho h\hat{U}} \tag{4}$$

where the wind stress τ_w (in dyn cm^{-2}) $\approx 0.04W^2$ (W in m s^{-1}), k the bed-stress coefficient ≈ 0.0025, $\hat{U}$ the background tidal amplitude $\approx$ 80 cm s^{-1}, g = 981 cm s^{-2}, ρ = 1 g cm^{-3} and H is the depth. Thus from (3) a mean wind-driven surface current of 17 cm s^{-1} requires a mean wind speed W of 16 m s^{-1} while U_w = 3 cm s^{-1} requires W = 7 m s^{-1}. These results again suggest that wind forcing alone is insufficient to account for the observed net residual currents.

In the southern region where depths are typically 20 m, from (4), a surface residual of 17 cm s^{-1} would require a density gradient $\rho^{-1}(\partial\rho/\partial x)$ of 2.5% · km^{-1}. In the northern region with depths up to 50 m, a surface residual of 3 cm s^{-1} requires $\rho^{-1}(\partial\rho/\partial x)$ = 0.07% · km^{-1}. Such density gradients are not entirely incompatible

with the likely pattern associated with the mixing of fresh water from the Conway estuary (located immediately west of the Orme radar site), however no direct observational evidence is available for direct validation.

b. Time varying residuals

To construct synoptic distributions of residual currents at hourly intervals both temporal and spatial interpolation was required. Linear spatial interpolation was used to derive values at the beam crossing points (as described for the tidal components). Quadratic temporal interpolation was then used to calculate values "on the hour" using the nearest three values in time. Figure 6 shows examples of two consecutive instantaneous residual current (i.e., observed minus tidally predicted) distributions, one hour apart. At the instant shown the wind speed (Fig. 10) is about 8 m s^{-1} slackening and veering from SE towards S.

Figure 7 shows the distribution of rms residual speeds obtained after removal of both the harmonically predicted tidal components and the time-averaged residuals shown in Fig. 5. These values range from about 7 cm s^{-1} in the northern region up to 15 cm s^{-1} in the shallower southern area. The equivalent value obtained from the bottom-mounted current meter at position A was 3.3 cm s^{-1}, and 5.6 cm s^{-1} from the mid depth mooring at position B. Figure 7 also shows the equivalent distribution of rms residual speeds obtained after the removal of remaining tidal energy by filtering with the Doodson Xo filter (Doodson and Warburg, 1941). This filter involves manipulation of hourly data extending up to 19 hours either side of the central time. It is highly effective in removing tidal energy in the diurnal, semidiurnal, quarter- and sexto-diurnal bands. One disadvantage of the filter is an aliasing of higher frequency energy producing an erroneous oscillation at a period of 2.6 h. This characteristic, clearly evident in subsequent time series, should be disregarded. From Fig. 7, we note that this filtering reduces the rms residual speeds from a mean of 11 cm s^{-1} to 4 cm s^{-1} and also significantly changes the spatial distribution. These consequences suggest a high level of interaction between the propagation of the tidal component and the surge component. To avoid the complexities of such interaction subsequent analyses of the residual currents are carried out using the filtered values. Figure 8 shows the filtered time series of OSCR current residuals at position A.

c. Response to wind forcing

Conceptually two alternative response modes relating surface currents to wind forcing were envisaged, one appropriate to nearshore and one to open-sea conditions.

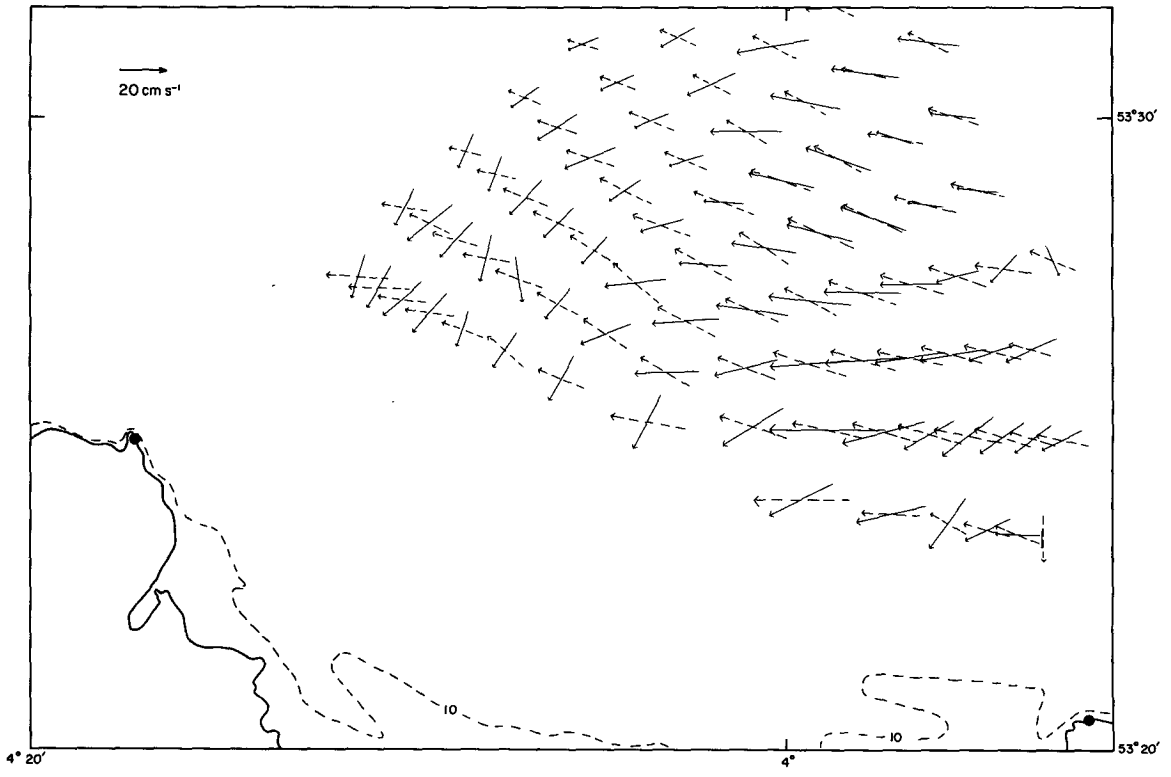

FIG. 6. Instantaneous residual circulation. Successive hourly values 22.00 (DASHED) and 23.00 25 May 1985.

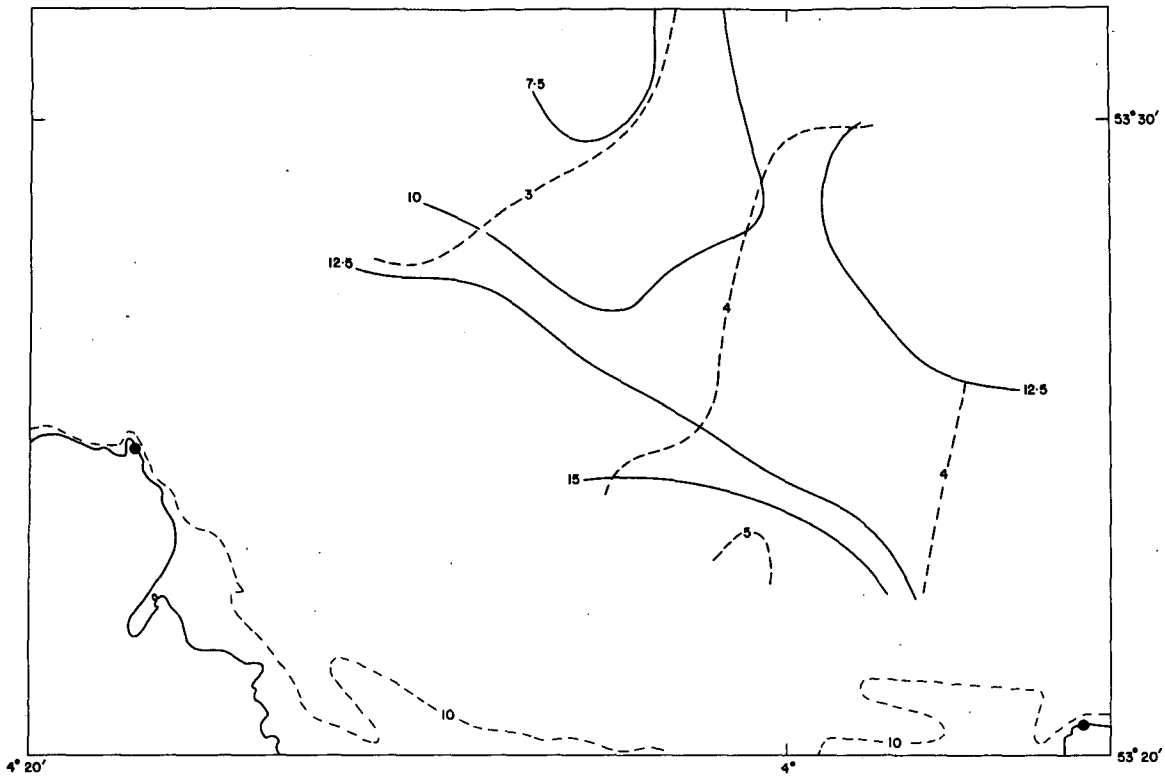

FIG. 7. Root-mean-square residual speed distribution (in cm s^{-1}). (a) —— harmonic tidal components removed, (b) - - - - - Doodson Xo filter applied to (a).

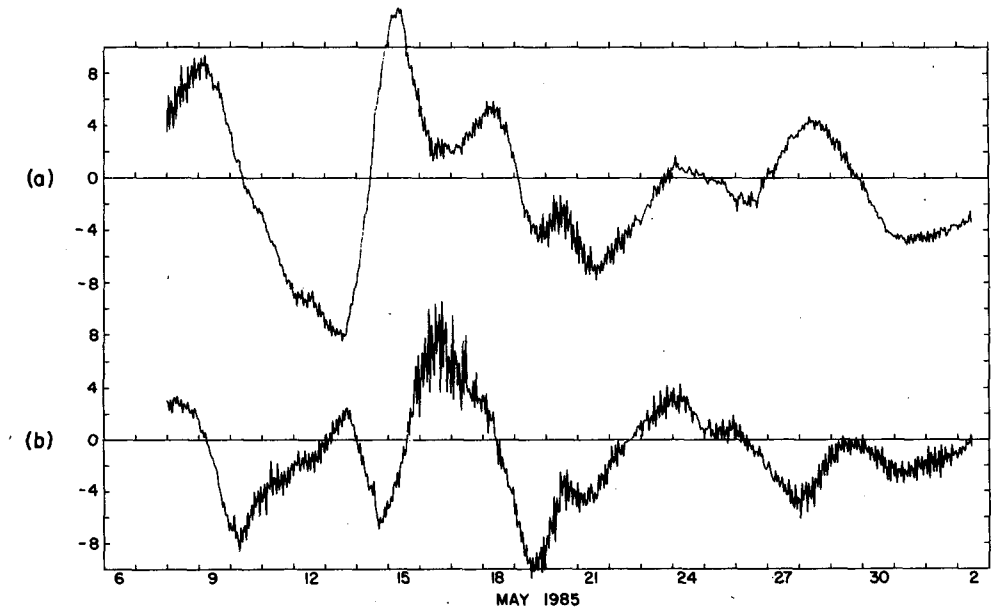

FIG. 8. Residual current components at position A (in cm s^{-1}) harmonic tidal component removed and Doodson Xo filter applied. (a) East–West and (b) North–South.

1) NEARSHORE RESPONSE

First, referring to Fig. 9a, nearshore the residuals might be expected to be preferentially oriented along the direction α (with α likely to be parallel to the shoreline or depth contours). The residual component along α, $R_\alpha = R\cos(\theta - \alpha)$ is then assumed to vary with the component of wind stress, $\tau_\beta = \tau\cos(\phi - \beta)$ resolved along some optimum direction β as follows:

$$R_\alpha = \bar{R} + a_1\tau_\beta. \tag{5}$$

The orthogonal components of wind stress are $\tau_x = bW_x(W_x^2 + W_y^2)^{1/2}$ and $\tau_y = bW_y(W_x^2 + W_y^2)^{1/2}$, where b is a drag coefficient, a_1 the regression coefficient, $\bar{R}$ a constant velocity independent of wind, and W_x and W_y wind speeds in m s^{-1} directed east and north respectively. Likewise residual velocities are U and V along the x and y axes. Then (5) may be transformed to

$$U\cos\alpha + V\sin\alpha = \bar{R} + a_1b(\tau_x'\cos\beta + \tau_y'\sin\beta) \tag{6}$$

where $\tau_x = b\tau_x'$ and $\tau_y = b\tau_y'$.

At each position the preferential orientation, α, was determined corresponding to the axis of maximum resolved residual variance. A mean value of $\alpha = 0°$ (due east) was obtained and for 60 out of 84 locations $350° < \alpha < 10°$. However, on examining the ratio of the variance along the α axes to the variance along the orthogonal axes, a mean ratio of about 2 and a maximum of 4 were calculated. Hence the alongshore residual flow concept does not seem appropriate. However, for completion, a least-squares fit to equation (6) was used to determine the parameters $\bar{R}$, a_1b and β. Hourly wind recordings from Valley (Fig. 1) were used (Fig. 10). A mean value of $a_1b = 0.0125$ was obtained (with W in m s^{-1} and R in cm s^{-1}) with a minimum of 0.005 at the western edge increasing systematically to 0.0135 at the eastern edge. The deflection angle between maximum residual variance and most effective wind direction showed a mean value close to 0° and was within the range ±10° at 79 out of 84 locations. Residual velocities along the α axis calculated from (6) accounted for only 35% of the observed residual variance along this axis.

2) OPEN SEA RESPONSE

In open-sea conditions it was envisaged that the residual surface current would be at some fixed angle ($\phi - \theta$) to the wind stress with a magnitude directly proportional to the wind stress. Thus, referring to Fig. 9b we assume

$$R_\theta = \bar{R} + a_2\tau_\phi \tag{7}$$

or

$$U + iV = U_0 + iV_0 + a_2b(\tau_x' + i\tau_y') \tag{8}$$

where $\bar{R} = (U_0 + iV_0)$ is a constant velocity independent of wind.

A least-squares fit to (8) produced mean magnitude for $a_2b = 0.04$ with $\phi - \theta = 20°$, this veering is in the direction expected from Ekman theory. Magnitudes of a_2b ranged from 0.03 at the northern edge to 0.05 in the south while at 76 out of 84 locations $10° < \phi - \theta < 30°$. Figure 10 shows the time series of wind speed squared (W^2) components resolved along 70° and 340°. These wind stress components force currents easterly and northerly, respectively. However, comparison of Fig. 10 with the residual components at position A (Fig. 8) shows limited correlation. Over the whole area, subtracting the current vectors calculated by (8) from the observed residuals only reduced the speed variance by 20%.

In a further attempt to relate the residual velocities to the wind vectors, separate relationships along the east–west and north–south axes were examined, namely

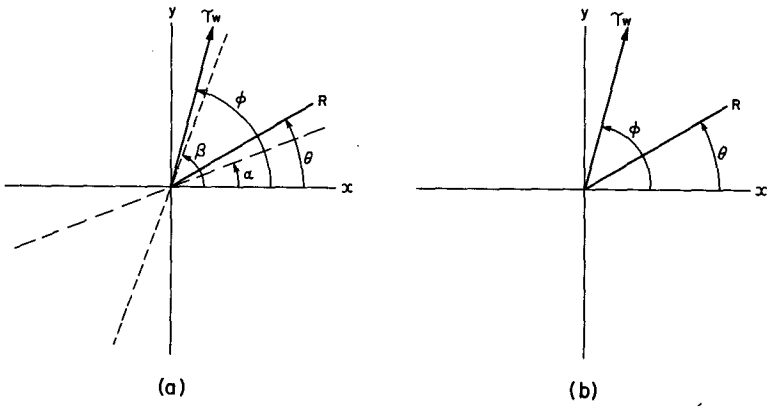

FIG. 9. Conceptual response between wind forcing and surface current residuals. (τ, ϕ) wind stress direction, (R, θ) residual current. (a) Nearshore response, residuals constrained to be aligned close to the axis α, and (b) open-sea response, residual currents veer ($\phi - \theta$) from wind stress direction.

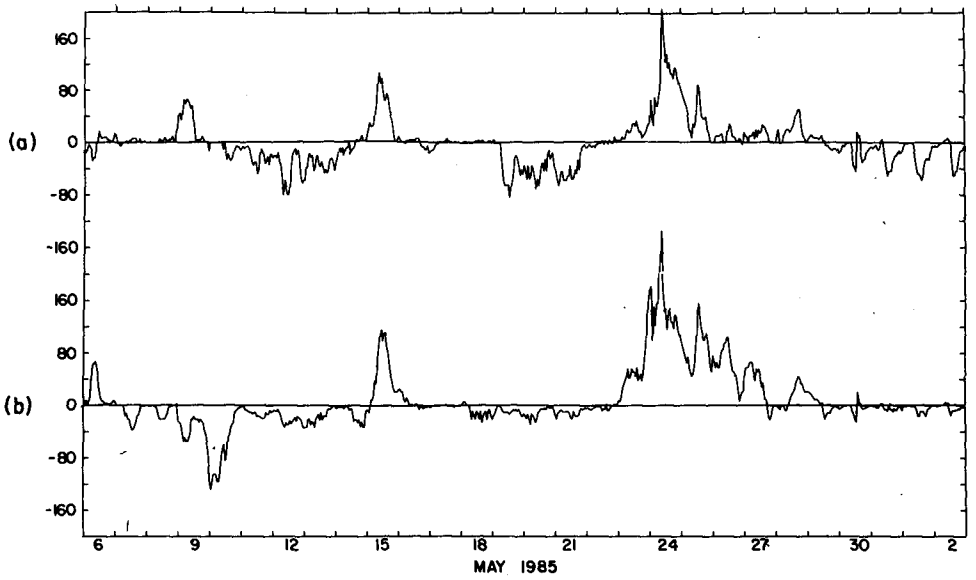

FIG. 10. Wind forcing components. Components of wind stress (W^2 in $m^2\ s^{-2}$) along directions (a) 70° and (b) 340° (clockwise from N). Calculations indicate these components are most effective in producing (a) easterly and (b) northerly current residuals.

E–W axes: $$u = \bar{u} + a_x\tau\cos(\phi - \alpha_x)$$
$$= \bar{u} + a_x b(\tau'_x\cos\alpha_x + \tau'_y\sin\alpha_x) \quad (9)$$

N–S axes: $$v = \bar{v} + a_y\tau\sin(\phi - \alpha_y)$$
$$= \bar{v} + a_y b(\tau'_y\cos\alpha_y - \tau'_x\sin\alpha_y). \quad (10)$$

Least-squares fit to (9) and (10) produced mean values of $a_x b = 0.1$, $a_y b = 0.03$, $\alpha_x = 0°$ and $\alpha_y = 30°$, thus indicating a significantly different response along the two axes. Average correlation factors between u and v calculated from (9) and (10) and the observed time series were 0.6 and 0.4.

The values of (a, b) calculated from these open-sea and nearshore responses may be compared to the 2% rule and to the formulation (3). For the mean-squared wind speed over the experiment of 36.2 $m^2\ s^{-1}$ the 2% rule reduces to

$$U_w = 0.33W^2. \quad (11)$$

For the conditions cited, Eq. (3) reduces to

$$U_w = 0.06W^2. \quad (12)$$

The mean values found from the formulations examined were, respectively, for (6) $a_1 b = 0.0125$, for (8) $a_2 b = 0.04$, for (9) $a_x b = 0.1$ and for (10) $a_y b = 0.03$.

In summary, the formulations (6), (8), (9) and (10) only account for a fraction of the observed residual currents, the magnitudes of the associated coefficients are compatible with (3) but significantly less than the 2% rule. The latter rule is probably more applicable to the higher frequency residual component—previously removed by filtering.

5. Empirical orthogonal functions (EOF)

In the previous section, only limited correlation was found between the residual current time-series and the corresponding wind forcing. The question than arises as to whether the remaining residual components, seemingly uncorrelated to wind forcing, are simply randomly distributed or are organized into some ordered motion. A rotary empirical orthogonal function (EOF) technique was used to analyze the spatial array of OSCR measurements with the aim of determining any organized patterns of motion, i.e., modes. Klinck (1985) provides a comprehensive description of the method; here we provide a brief outline (see also Kundu and Allen, 1976).

The data series (filtered Xo version) is stored in a complex array $W(j, k)$, where j represents the hourly time series 1 to N and k the locations 1 to M.

$$W_{j,k} = U_{j,k} - \bar{U}_k + i(V_{j,k} - \bar{V}_k) \quad (13)$$

where U and V are easterly and northerly residual components. The Hermitian matrix $\mathbf{H}$ is formed as follows

$$\mathbf{H} = \frac{1}{N}\mathbf{W}\cdot\mathbf{W}^{\mathrm{T}} \quad (14)$$

where $\mathbf{W}^{\mathrm{T}}$ is the complex conjugate transpose of $\mathbf{W}$. The eigenvalues λ_m and eigenvectors e_m of $\mathbf{H}$ are computed, satisfying

$$\mathbf{H}e_m = \lambda_m e_m. \quad (15)$$

A complex series A_{jm} for the mth mode EOF is then calculated from

$$A_{j,m} = \sum_{k=1}^{M} W_{j,k} e^*_{m,k} \quad (16)$$

where e^*_m is the complex conjugate of e_m. The array **W** contained the residuals from all 84 locations, mean values of U and V were removed but the data were not normalized. Because of limitations in computer memory size, the above analysis was carried out in three sections each comprising 168 hourly datasets. For the most energetic modes, the velocity vectors computed in the three sections were almost identical and henceforth, no consideration will be given to the small differences between the three separate analyses.

Figure 11 shows the percentage of the total variance at all 84 locations accounted for by the first 10 EOF modes. Mode 1 accounts for 66% of the total variance, mode 2 accounts for 8% and successive modes all less than 4% each. The velocity vectors from mode 1 are shown in Fig. 12 and the time series A_1 of the (complex) amplitude is shown in Fig. 13. In view of the overwhelming contribution of mode 1, further consideration will be restricted to this mode. The velocity vectors for this mode are close to a uniform alignment with deviations rarely more than ±20° of the mean direction. The magnitudes of these velocity vectors vary systematically with a minimum of 0.65 (expressed as a fraction of the overall mean) at the western edge up to a maximum of 1.3 close to the eastern edge. This magnitude distribution is correlated with the distribution for percentage variance accounted for by mode 1, the latter reaches a peak of almost 90% close to the eastern edge.

The time series for A_1 (Fig. 13) shows excellent correlation with the residual current time series at position A shown in Fig. 8. (Strictly the modal time series A_1 cannot be simply resolved into N–S and E–W axes. However, because in this case the velocity vectors are close to a uniform alignment, it is both reasonable and of direct interest to translate the complex components of A_1 into these orthogonal spatial axes.) The extent of this correlation can be measured from the 84% of total variance at this location accounted for by mode 1. However comparison of the time series for A_1 with the effective wind stress components shown in Fig. 10 indicates only limited correlation. To investigate the relationship between the time series for A_1 and that for wind stress, the following relationship was assumed:

$$A_1 - \bar{A}_1 = r(W_E^2 + iW_N^2) \quad (17)$$

where $\bar{A}_1$ is a constant component in A_1.

By least-squares fitting, a value r = (0.062, 29°) (A_1 in cm s^{-1}, W_E and W_N in m s^{-1}) was calculated, indicating a veering direction between surface current and wind of 29°.

The value of 0.062 for the amplitude of r may be compared to the mean values for $a_1 b$ = 0.0125, $a_2 b$ = 0.04, $a_x b$ = 0.1 and $a_y b$ = 0.03 deduced from Eqs. (6), (8), (9) and (10). This similarity in magnitude suggests that wind forcing may be primarily responsible for the observed residuals, but a complex asymmetric relationship may be involved including significant variable time lags.

Correlation of the orthogonal components for $\bar{A}_1 + r(W_E^2 + iW_N^2)$ calculated from (17) with the original time series, A_1, produced values of 0.73 along the E–W axis and 0.32 along the N–S axis. This 0.73 correlation coefficient for the E–W axis exceeds the correlation coefficient of 0.60 calculated earlier [Eq. (9)] between the E–W component of residual velocity and the corresponding optimal wind stress component. The opposite result is found for N–S components (0.32 against 0.4). A time variation in the large mean N–S residual (perhaps a changing density field due to winds or river flow fluctuations) might be the reason for the lower correlation along this axis.

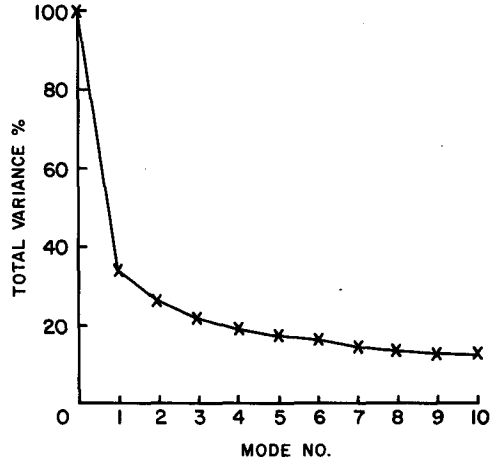

FIG. 11. Percentage of total (filtered) residual variance accounted for by successive subtraction of EOF modes 1 to 10.

6. Discussion and conclusions

This OSCR experiment has resulted in a unique data set revealing details of the fine scale spatial distribution of near-shore surface currents. The data were separated into tidal and nontidal motions, which permitted the validity of the observations to be established and the subsequent analysis to be performed.

Treating first the tidal components, the exceptionally smooth and regular spatial distribution of the predominant M_2 tidal ellipses are mutally consistent to a precision of better than 0.5 cm s^{-1} in the amplitude of the major axis. Statistical analyses of these results indicate that the standard error for OSCR current measurements is less than 4 cm s^{-1}. Comparison, at one location, of the M_2 surface results with data from current meters moored (a) at middepth and (b) near-bed, further confirmed the validity of the OSCR measurements. However, one uncertainty concerning the focussing of OSCR (i.e., the extent to which results from a specific

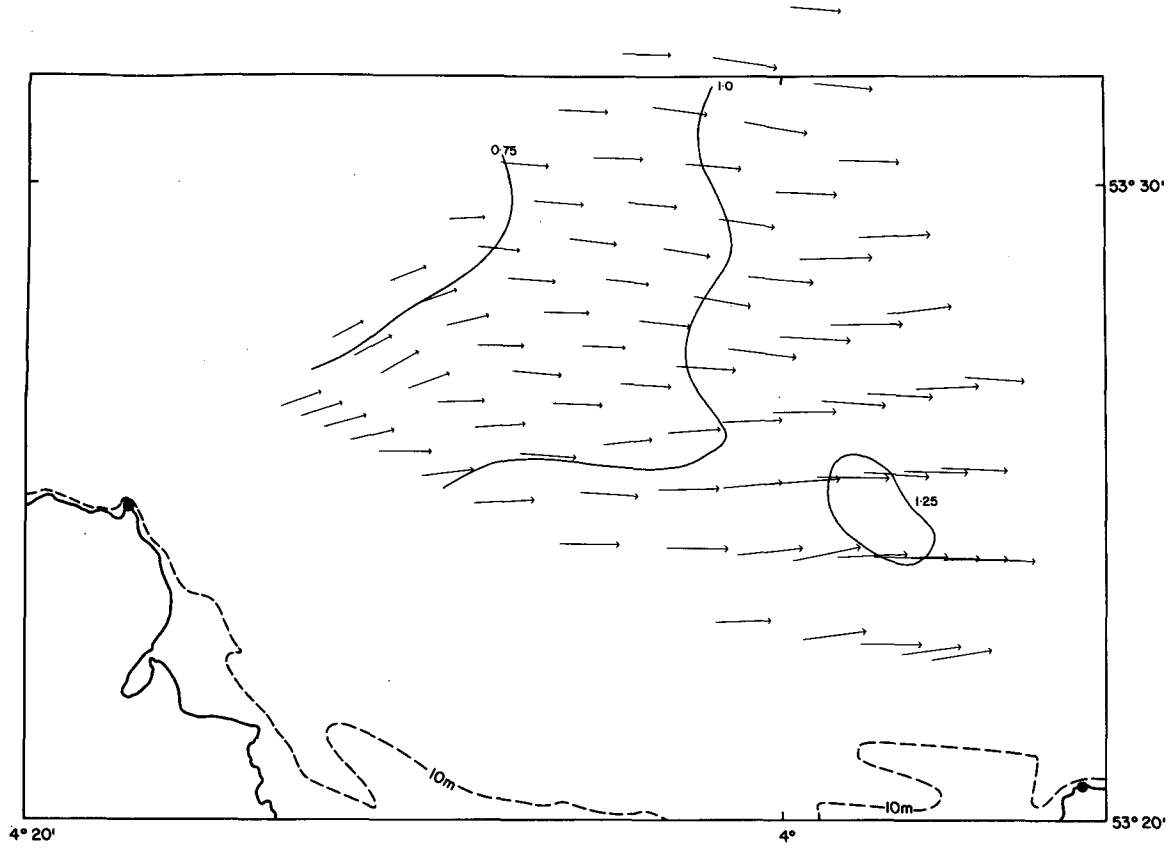

FIG. 12. Velocity vectors for EOF mode 1. Contours show current amplitude as a fraction of the overall mean.

bin and beam reflect conditions pertaining solely to that region) remained. Indeed, considered in isolation, the smoothness of the M_2 results might suggest a lack of focussing with a specific ellipse reflecting conditions over an area much larger than the bin and beam concerned.

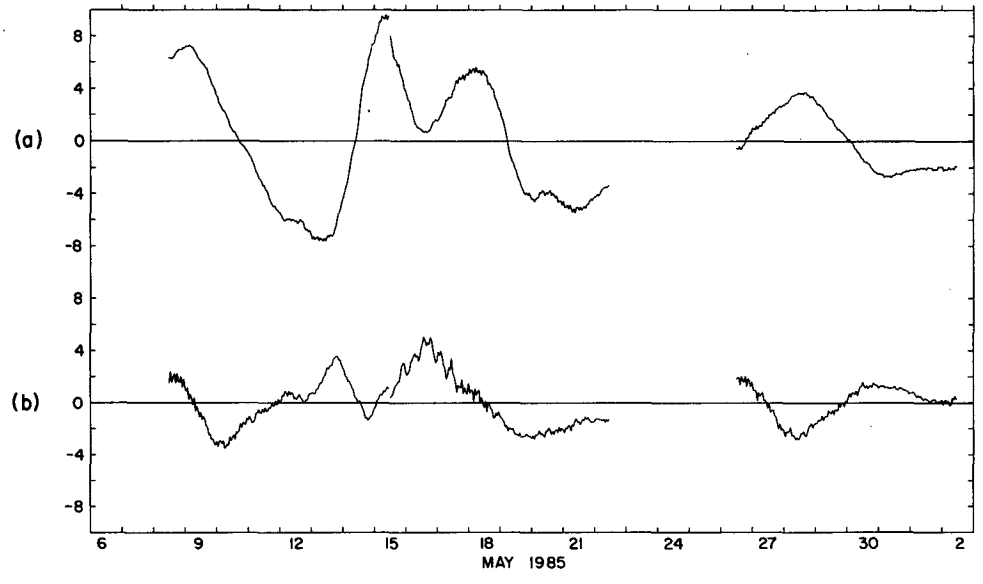

FIG. 13. Modal amplitude time series, A_1 (in cm s^{-1}) for EOF mode 1: (a) real (approx E–W) and (b) imaginary (approx N–S).

The pronounced but ordered spatial variability found for the major higher harmonic constituent M_4 clearly established the accurate focussing capability of OSCR. In combination, these results for the M_2 and M_4 constituents provide both concrete conclusions and challenging questions. Thus, from the smooth sweep of the M_2 currents, apparently insensitive to the finer topographic features, we readily appreciate how even coarse grid numerical models can accurately simulate the propagation of this constituent. By contrast, a major challenge is posed in providing an explanation of processes responsible for the complex M_4 current distribution.

The residual currents proved interesting in two respects. First, the large mean residual currents indicated a coherent northward surface transport. While the most likely driving mechanism appeared to be horizontal density gradients, a lack of density measurements precluded further investigation. The possibility of using OSCR in a future experiment to explore such mechanisms clearly suggests itself. Second, the relationship between the time-varying residual currents and the most likely driving force, namely surface wind stress, proved both tantalizing and revealing.

In examining separately the relationship between the residual current time series at each position with the wind-stress time series, only limited correlation was obtained. While the magnitude of the calculated responses was of the expected order, there remained a large part of the residual signal seemingly unconnected with direct wind forcing. The question then arose as to whether the non-wind driven residuals were random or part of an ordered motion.

An empirical orthogonal function analysis was used to determine modal distributions. This revealed a single mode accounting for 66% of the total residual variance. The spatial structure of this mode indicated uniform alignment (within ±20°) with ordered amplitude variations of up to ±30% of the mean value. Moreover, the areas of maximum modal amplitude corresponded to the areas of maximum residual variance contained within this first mode. The time series of the complex modal amplitude (by which this mode is multiplied to obtain a residual time series at each location) showed a correlation with the wind stress time series of 0.73 along the E–W axis and 0.32 along the N–S axis with an overall veering of 29° clockwise between the modal current and wind directions. The modal amplitude time series is largely free from high frequency components evident in the wind-stress signal (filter aliasing indicates energy at a period of 2.6 h which should be ignored) and is characterized by oscillations in the period range from 4 to 7 days. The tidal filtering effectively removes frequencies of less than one day. These longer period oscillations must be related to larger horizontal scale motions or perhaps to a slowly developing vertical current profile associated with gradual changes in the density field. Thus, a low-frequency slablike surface current response to wind forcing is indicated. The spatial variation in the amplitude of this conceptual response might be attributed to a breakdown of the "slab" in nearcoastal regions with a change in the vertical current structure. Such a change in vertical structure might be expected nearshore where wind stress may be balanced by surface gradients (that act uniformly through the water depth) rather than simply by surface currents as in open-sea conditions.

Acknowledgments. This work was funded by the Natural Environment Research Council. The support of J. Simpson, University College of North Wales, and P. Linden, University of Cambridge, who were involved in simultaneous field programs, is gratefully acknowledged. Technical support from the Rutherford–Appleton Laboratory team (headed by D. Eccles) responsible for the OSCR design is also duly acknowledged. The success of the experiment follows directly from the enthusiastic diligence shown by a large number of colleagues from I.O.S. at all stages from planning, through execution to the data processing stages. The wide range of these contributions makes it difficult to single out individuals here but their efforts must be recognized and are heartily appreciated.

REFERENCES

Barrick, D. E., 1978: H. F. radio oceanography—a review. *Bound.-Layer Meteor.*, **13**, 23–43.

——, M. W. Evans and B. L. Weber, 1977: Ocean surface currents mapped by radar. *Science*, **198**, 138–144.

Doodson, A. T., and H. Warburg, 1941: *Admiralty Manual of Tides.* H.M.S.O., London, 270 pp.

Godin, G., 1972: *The Analysis of Tides.* Liverpool University Press, 264 pp.

King, J. W., and co-authors 1984: OSCR (Ocean Surface Current Radar) observations of currents off the coasts of Northern Ireland, England, Wales and Scotland. Current measurements offshore. Soc. Underwater Technol., London, 38 pp.

Klinck, J. M., 1985: EOF analysis of central Drake Passage currents from DRAKE 79. *J. Phys. Oceanogr.*, **15**, 288–298.

Kundu, P. K., and J. S. Allen, 1976: Some three-dimensional characteristics of low-frequency current fluctuations near the Oregon Coast. *J. Phys. Oceanogr.*, **6**, 181–199.

Leise, J. A., 1984: The analysis and digital signal processing of NOAA's surface current mapping system. *IEEE J. Oceanic Eng.*, **OE-9**, 106–113.

Pingree, R. D., and L. Maddock, 1985: Stokes Euler and Lagrange aspects of residual tidal transports in the English Channel and the Southern Bight of the North Sea. *J. Mar. Biol. Assoc. U.K.*, **65**, 969–982.

Prandle, D., 1982: The vertical structure of tidal currents and other oscillatory flows. *Contin. Shelf Res.*, **1**, 191–207.

——, 1985a: On salinity regimes and the vertical structure of residual flows in narrow tidal estuaries. *Estuarine, Coastal Shelf Sci.*, **20**, 615–635.

——, 1985b: Measuring Currents at the Sea Surface by H.F. Radar (OSCR). *J. Soc. Underwater Technol.*, **11**(2), 25–27.

——, and D. K. Ryder, 1985: Measurement of surface current in Liverpool Bay by high-frequency radar. *Nature*, **315**(6015), 128–131.

——, and J. Howarth, 1986: The use of HF radar measurements of surface currents for coastal engineers. *Int. Conf. on Measuring Techniques of Hydraulics Phenomena in Offshore Coastal and Inland Waters.* London, B.H.R.A. Cranfield.

Robinson, I. S., 1979: The tidal dynamics of the Irish and Celtic Seas. *Geophys. J. Roy. Astron. Soc.*, **56**, 159–197.

Shearman, E. D. R., 1983: Propagation and scattering in m.f./h.f. groundwave radar. *IEE Proc.* (F), **130**, 579–590.